Magnetic scanning gate microscopy of CoFeB lateral spin valve

Héctor Corte-León, Alexander Fernandez Scarioni, Rhodri Mansell, Patryk Krzysteczko, David Cox, Damien McGrouther, Stephen McVitie, Russell Cowburn, Hans W. Schumacher, Vladimir Antonov, and Olga Kazakova

Citation: AIP Advances **7**, 056808 (2017); doi: 10.1063/1.4977891
View online: http://dx.doi.org/10.1063/1.4977891
View Table of Contents: http://aip.scitation.org/toc/adv/7/5
Published by the American Institute of Physics

AIP ADVANCES 7, 056808 (2017)

Magnetic scanning gate microscopy of CoFeB lateral spin valve

Héctor Corte-León,[1,2,a] Alexander Fernandez Scarioni,[3] Rhodri Mansell,[4] Patryk Krzysteczko,[3] David Cox,[1,5] Damien McGrouther,[6] Stephen McVitie,[6] Russell Cowburn,[4] Hans W. Schumacher,[3] Vladimir Antonov,[2] and Olga Kazakova[1]

[1]*National Physical Laboratory, Teddington TW11 0LW, United Kingdom*
[2]*Royal Holloway University of London, Egham TW20 0EX, United Kingdom*
[3]*Physikalisch-Technische Bundesanstalt, Braunschweig D-38116, Germany*
[4]*Cavendish Laboratory, University of Cambridge, Cambridge CB3 0HE, United Kingdom*
[5]*Advanced Technology Institute, University of Surrey, Guildford GU2 7XH, United Kingdom*
[6]*Department of Physics and Astronomy, University of Glasgow, Glasgow G12 8QQ, United Kingdom*

(Presented 2 November 2016; received 23 September 2016; accepted 30 November 2016; published online 1 March 2017)

Devices comprised of CoFeB nanostructures with perpendicular magnetic anisotropy and non-magnetic Ta channel were operated in thermal lateral spin valve (LSV) mode and studied by magnetotransport measurements and magnetic scanning gate microscopy (SGM). Due to the short spin diffusion length of Ta, the spin diffusion signal was suppressed, allowing the study of the contribution from the anomalous Nernst (ANE) and anomalous Hall effects (AHE). The magnetotransport measurements identified the switching fields of the CoFeB nanostructures and demonstrated a combination of AHE and ANE when the devices were operated in thermally-driven spin-injection mode. Modified scanning probe microscopy probes were fabricated by placing a NdFeB magnetic bead (MB) on the apex of a commercial Si probe. The dipole magnetic field distribution around the MB was characterized by using differential phase contrast technique and direct measurement of the switching field induced by the bead in the CoFeB nanodevices. Using SGM we demonstrate the influence of localized magnetic field on the CoFeB nanostructures near the non-magnetic channel. This approach provides a promising route towards the study of thermal and spin diffusion effects using local magnetic fields. [http://dx.doi.org/10.1063/1.4977891]

I. INTRODUCTION

Lateral spin valves (LSVs), comprised of two ferromagnets connected by a non-magnetic channel, play a central role in spintronics due to their potential to create spin currents enabling a new range of spintronic devices.[1] In particular, they have a potential to replace actual hard drive reading heads.[2] It has also been demonstrated that the thermally-driven LSVs[1–4] produces much more efficient spin-injection per unit of current than the more common charge current spin-injection.[5] However, when operated in the thermal mode, depending on the magnetization direction, LSV also exhibits other effects such as the anomalous Nernst effect (ANE) or the anomalous Hall effect (AHE) that superimpose with the spin signal. For these reasons, it is essential to perform comprehensive characterization of the heat and spin transport across the non-magnetic channel.

When a LSV is operated in thermal mode, charge current I is passed through one of the magnetic elements (between contacts 3 and 4 in Fig. 1(a)), creating a spin accumulation in the non-magnetic

[a]Author to whom correspondence should be addressed. Electronic mail: hector.corte@npl.co.uk

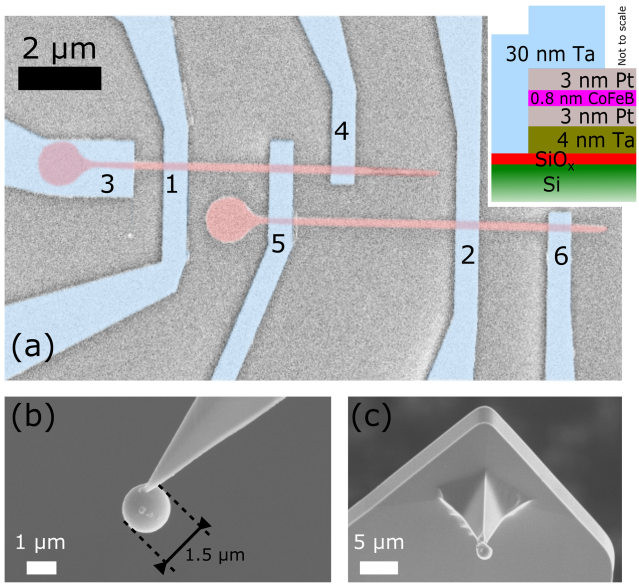

FIG. 1. (a) False color SEM image of the LSV with numbered electrical contacts. Inset: stack composition. (b)-(c) An AFM probe modified with a NdFeB MB attached at the apex.

channel and generating Joule heating both in the ferromagnet and the non-magnetic channel (contact 5 in Fig. 1(a)). The resulting heat gradient facilitates the spin diffusion through the non-magnetic channel and generates a potential difference between the channel and the second ferromagnet (contacts 5 and 6 in Fig. 1(a)) due to the imbalance between populations of electrons with spins up and down. In materials with perpendicular magnetic anisotropy (PMA), such as Pt/CoFeB/Pt studied here, the heat gradient created in this way also contributes to the ANE,[6] *i.e.* the current in the first ferromagnet creates a temperature gradient perpendicular to the external out-of-plane magnetic field, thus an electrical field orthogonal to both appears. In addition to ANE effect, PMA materials also exhibits the AHE, which in the LSV geometry can contribute to the final output voltage.

Here, we use magnetic scanning gate microscopy (SGM) to study the effect of local magnetic fields[7,8] on a LSV device composed of ultra-thin CoFeB magnetic nanostructures and non-magnetic Ta channel. The LSV is operated in the thermal mode, where the Ta channel suppresses the spin signal,[9] leaving only the ANE and AHE contributions. Using a modified probe with a NdFeB magnetic bead (MB), we study the effect of a local magnetic field on the CoFeB nanostructures near the non-magnetic channel. To estimate the absolute value of the bead's stray magnetic field, the differential phase contrast (DPC) technique was applied and the results were compared with the estimated values extracted from SGM measurements. This approach can be further used for LSV with channels made of other materials to distinguish the spin-current contribution along the non-magnetic channel.

II. EXPERIMENTAL METHODS

The magnetic elements of LSVs were fabricated from a continuous polycrystalline multilayer film with stack composition Ta(4 nm)/Pt(3 nm)/$Co_{60}Fe_{20}B_{20}$(0.6 nm)/Pt(3 nm) deposited by successive sputtering in an unbroken vacuum at $0.5x10^{-7}$ mbar on Si/SiO_2(1000 nm) substrate. Each LSV was comprised of two magnetic nanostructures and a non-magnetic channel. Magnetic elements were fabricated using standard e-beam lithography and negative resist process with Ar etching. The nanostructures are 6 μm in length and 200 nm in width, with one tapered end (forming a 15° angle in the top nanostructure and a 60° angle in the bottom one, see Fig. 1(a)) and a disk of 1 μm in diameter at another end. In PMA nanostructures, the tapered end acts as a nucleation point for magnetization reversal, where sharper tapered ends enable lower coercive field.[10,11] Different coercive fields for each device are important as they allow to investigate the device in parallel and antiparallel configurations. A non-magnetic channel between the magnetic elements and electrical contacts on the sample were

prepared in two steps using a positive resist process and sputtering deposition. In the first step, the electrical contacts with the sample were fabricated first by cleaning the contact area using oxygen plasma, then after breaking the vacuum the Ta (30 nm) layer was deposited. In the second step, large electrical pads for wire bonding were fabricated by mild Ar etching and deposition of Ta (5 nm) and Au (100 nm) layers. The resulting non-magnetic Ta channel connecting the ferromagnetic structures is 1 μm in length and 500 nm in width. The small spin-diffusion length in Ta, ~1 - 2 nm, reported previously[15] suppresses the spin diffusion between the two magnetic nanostructures.

Magnetotransport measurements were performed in different electrical schemes (Fig. 2(b)) in an out-of-plane magnetic field using a DC current (I = 502 μA) at room temperature. The output voltage was measured using a nanovoltmeter with 10 powerline cycles (PLC) as an integration time (*i.e.* each PLC is 20 ms long and the total integration time is 200 ms per measurement).

The scanning probe microscopy (SPM) system (Aura, NT-MDT with home-built transport measurement stage) was used for magnetic SGM studies in ambient conditions. The system allows application of an out-of-plane magnetic field during scanning as well as electrical connections to the sample. In SGM mode, the sample's topography is recorded in non-contact mode simultaneously with measurements of the voltage across the sample. To minimize the electrostatic interactions,

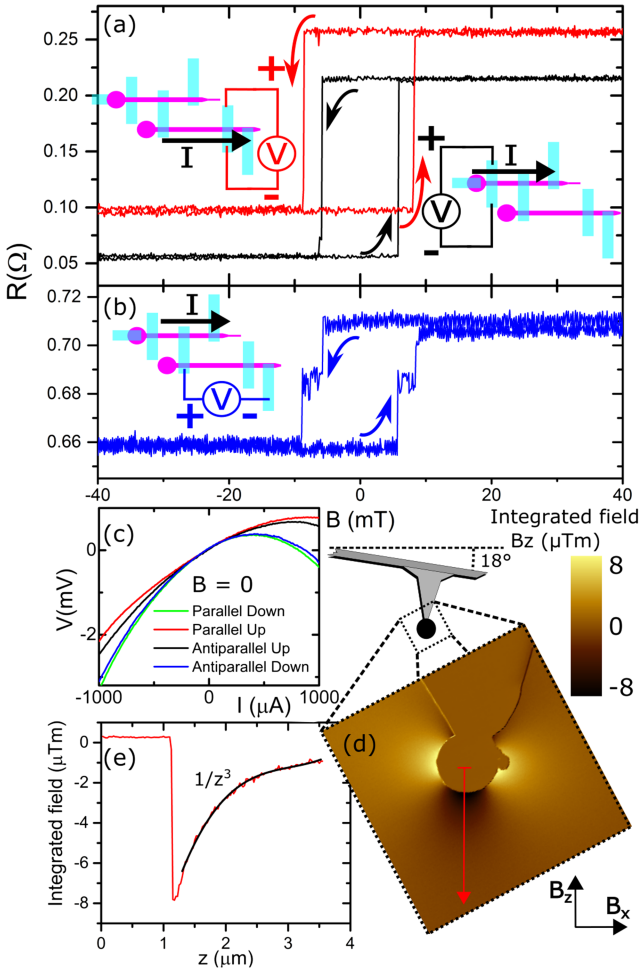

FIG. 2. (a) Magnetotransport measurements of the AHE measured at crosses 1 and 2. (b) Magnetotransport measurements in the thermal LSV configuration (*i.e.* current passed between contacts 3 and 4, voltage measured between contacts 5 and 6, see Fig. 1(a) for reference). (c) Variation of the voltage in respect to the applied current at zero field for four magnetization states, demonstrating combination of linear and quadratic components. (d) DPC image of the modified probe, the color indicates the value of the integrated field along B_z direction. (e) Profile extracted from the red line in (d) with $1/z^3$ fitting shown in black.

the probe was grounded. The resistance was measured using the same electrical circuit as for the magnetotransport measurements.

The modified probes used in SGM (Fig. 1(c)) were custom-made by removing the apex of a commercial silicon AFM probe (TESPA V2, Bruker) and placing a MB on the flattened pyramid using a FIB system equipped with micromanipulators and a Pt-based deposition to glue the MB (Fig. 1 (b–c)).[12] Here, we used commercial magnetic NdFeB microspheres (MQP-S-11-9-20001-070 Isotropic Powder[13]) with diameter of ~1.5 μm (Fig. 1(b)). Prior to the experiment, the modified probes were magnetized by applying a magnetic field of ~2 T perpendicular to the cantilever (*i.e.* stray field pointing towards +z direction in Figs. 2(d) and 3(a)).

DPC is a scanning tunneling electron microscopy (STEM) method where the electron beam is focused in the specimen plane and a quadrant detector is situated in the far field. The deflection, β, of the electron beam (of wavelength λ) is directly related to the magnetic induction component perpendicular to the beam integrated along the beam path:[14–16]

$$\beta = \frac{e\lambda}{h}\int_{-\infty}^{\infty} B_{\perp} dl \tag{1}$$

By taking the difference between the signals from opposite segments of the detector, components of the integrated induction are determined. This technique was previously used to image the magnetic field around standard MFM probes[16] and is used here to image the magnetic field distribution around the MB (Fig. 2(f)). The images were acquired on a JEOL ARM 200CF instrument equipped with a

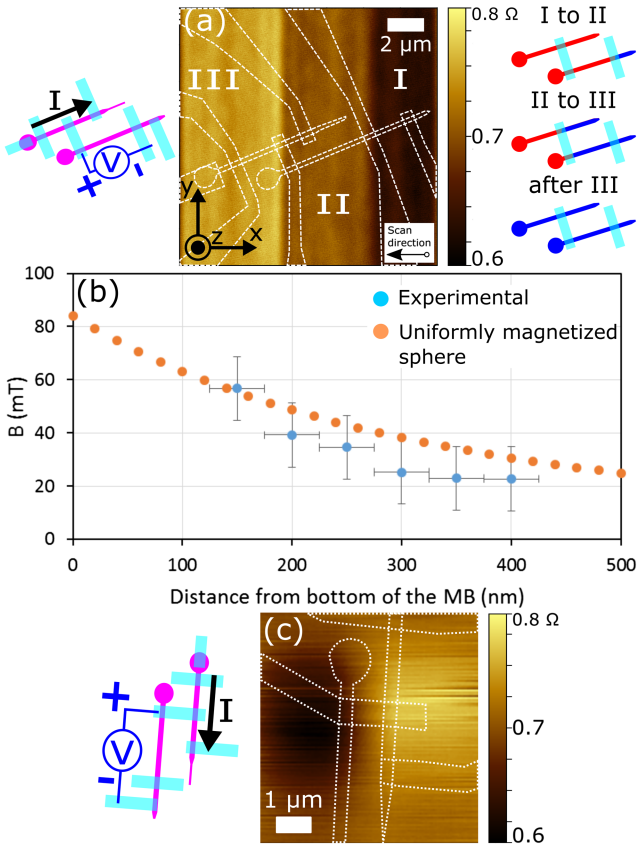

FIG. 3. (a) SGM image of the device in the thermal LSV configuration, no external filed applied. Numbers I to III indicate the different regions of the device magnetization. Left inset: electrical circuit. Right inset: magnetization of the magnetic elements in -z/+z (red/blue) orientation when the probe reaches the boundary of each region. (b) Measured magnetic field from the MB and calculated values for the field created by a sphere of the same radius. (c) SGM image of the non-magnetic channel in thermal LSV configuration, when a positive magnetic field is being applied to prevent remagnetization of magnetic elements.

probe aberration corrector and a cold field emission gun. The imaging conditions used in this instance were with a condenser aperture of radius 10 microns which corresponds to an imaging resolution of 3 nm.

III. RESULTS

Experimental results are divided into three parts. First, we perform the electrical characterization of the devices by means of magnetotransport measurements using out-of-plane magnetic field. Second, DPC measurements of the modified probes have been performed and the magnetic field distribution and intensity around the MB have been estimated. Finally, by performing SGM measurements with no applied field we show that the probe remagnetizes the CoFeB nanostructures, while by applying the external magnetic field, the probe's stray field is partially compensated allowing its effect on the magnetic nanostructures near the non-magnetic channel to be studied.

A. Magnetotransport characterization of the device

Magnetotransport measurements have been performed in the presence of an out-of-plane external magnetic field. The resulting field dependence of the resistance is shown in Fig. 2(a–b). Figure 2(a) shows the AHE signals at crosses 1 and 2 (see Fig. 1(a) for contacts reference) as black and red lines, respectively, when a current passes from contact 3 to 4 (black) or from contact 5 to 6 (red). As expected, Fig. 2(a) shows a hysteresis loop with two characteristic values of magnetoresistance (*i.e.* corresponding to the magnetization up/down). The change in the resistance is ~ 0.15 Ω and the background resistance is ~ 0.100-0.125 Ω. The different tapered ends (*i.e.* 15°/60° angles) result in different coercive fields for the magnetic elements. Figure 2(b) shows the resistance in the thermal LSV configuration, where the current is passed between contacts 3 and 4 of the top magnetic structure (*i.e.* emitter) and the voltage is measured between contacts 5 and 6 of the bottom magnetic structure (*i.e.* detector, see Fig. 1(a) for reference). The steps on the blue curve (Fig. 2(b)) match the magnetization reversal of each device (*i.e.* steps on the black and red curves in Fig. 2(a)), with a total change in resistance of ~ 0.05 Ω and a background resistance of about ~ 0.69 Ω. The double-step switching originates in the combination of the ANE produced by the heat transmitted from the emitter to the detector through the non-magnetic channel and the AHE from the emitter. It is possible to identify and separate the two effects as the ANE is quadratic, while the AHE is linear with current. Figure 2(c) demonstrates that the total signal is a combination of quadratic and linear responses.

B. DPC images and the field near the probe

Figure 2(d) shows a DPC image of the modified probe. As DPC measures only the integrated field perpendicular to the detector (Eq. 1), Fig. 2(d) demonstrates the intensity of the integrated B_z component of the field (analogous image for the B_x component is not shown). Figure 2(e) shows profile along the z-direction (*i.e.* perpendicular to the sample). The field distribution is very similar to the one produced by a uniformly magnetized sphere. Hence outside the sphere with radius, R, it is the same field distribution as from a magnetic dipole with moment **m** at a position **r**, with r>R:

$$\boldsymbol{B} = \frac{1}{4\pi}\left(\frac{3\boldsymbol{r}(\boldsymbol{m}\cdot\boldsymbol{r})}{r^5} - \frac{\boldsymbol{m}}{r^3}\right) \tag{2}$$

The field of the magnetic dipole decays as $1/z^3$ along the dipole direction. As shown in Fig. 2(e) black line, the integrated field seen in the DPC images has the same decay dependency, and hence the field produced by the MB can be approximated by a dipole.

C. SGM of the thermal LSV

Figure 3(a) shows an SGM image taken with the modified probe in non-contact mode. The probe oscillates at a resonant frequency of 352 kHz with an oscillation amplitude of 400 nm peak-to-peak (*i.e.* the average distance between the device and bottom of the probe is 200 nm). The resistance across the device is measured in the thermal LSV configuration (see inset in Fig. 2b) and is synchronized with the probe position over the sample. Before scanning, the device is saturated with a field pointing in –z direction (Fig. 3(a)). During the scan, the external field is set to zero and the field from the

MB is pointing in +z direction. The probe scans from +x to –x (*i.e.* from right to left). As the probe scans over the device, it produces changes in the thermal LSV signal creating three regions of clearly distinguished resistance, marked I, II, and III in Fig. 3(a). During the scanning, the probe remagnetizes consecutive parts of magnetic elements from –z to +z magnetization (*i.e.* from red to blue in Fig. 3(a) right-hand side schematics). These changes in magnetization only appear in the thermal LSV signal when the MB reaches electrical contacts (*i.e.* first contact 2 and then contact 5). Initially in region I, the probe remagnetizes the tapered end of the bottom element, with no effect on the resistance ~ 0.6 Ω, as this part of the device does not contribute to the electrical signal. As the MB (and the induced change in magnetization) reaches contact 2, the resistance increases up to ~ 0.7 Ω and the device is region II. In region III, after the probe passes contact 5, the resistance increases up to ~ 0.8 Ω and does not change anymore, as the remaining parts of both magnetic structures are being magnetized in +z direction. By repeating the scan in both directions no further changes are observed, as the device is now fully magnetized in the direction of the MB's stray field.

Thus, in this experiment, the MB remagnetizes the device preventing observation of any possible local effects. Similar problem is faced when using a commercial MFM probe. One of the main advantages of using the modified probe is its spherical shape, which leads to a less complex and much more symmetrical field distribution than the one from a commercial MFM probe. Additionally, it allows to tailor the coercive field of the probe. For example, in the case presented here the coercive field of the modified probe is much higher (~840 mT)[8] than that of a commercial probe(~7.5 - 65 mT).[17]

In order to partly compensate for the magnetic field of the probe and be able to perform SGM over the channel without remagnetizing the device, the magnetic field produced by the modified probe was estimated. First, the device was saturated in –z direction, then, without removing the external field, it was scanned with the MB (saturated in +z direction). By reducing the external field step-by-step in each scan, it was possible to find the external field value where the device switches magnetization, which means that the field from the MB plus the external field (pointed in opposite directions) are equal to the coercive field of the device (10 mT for cross 2 as extracted from the switching field of the red curve in Fig. 2(a)). Using this method and monitoring the AHE signal at cross 2, the stray field of the modified probe has been estimated for several distances between the top of the device and the bottom of the probe (Fig. 3(b)). Because the coercive field of the device was measured in a uniform field, whereas the field from the probe is non-uniform and the probe is oscillating, some difference between the measured and real field could be expected. However the larger size of the MB compared with size of the device allows the field to be considered as being uniform with a good degree of approximation. Variations of the field produced by the oscillation of the probe are addressed by the fact that the probe oscillation amplitude was about 15 nm peak-to-peak, while the closest average distance between the bottom of the MB and the top of the device was 100 nm. In order to further minimize possible variations, the measurements were performed several times and the error bars take into account the dispersion of the results. The values for a uniformly magnetized sphere with diameter 1.5 μm and moment ~3.66×10^{-13} Am^2 have also been plotted on the same graph. These results were calculated with (Eq. 2) using remanent magnetization and density of NdFeB powder,[9,11] *i.e.* M_r = 57.60 Am^2/kg and ρ = 3600 kg/m^3, respectively. The dipole approximation, the validity of which was confirmed by the DPC technique, and the measured field values agree very well, *e.g.* providing ~85 mT at the surface and ~40 mT at 200 nm away from the surface of the MB, allowing to properly compensate the field produced by the modified probe. It is noteworthy that the stray field from commercial probes[17] ranges from ~ 32 to ~ 73 mT at 50 nm.

Figure 3(c) shows an SGM image of the non-magnetic channel taken with the modified probe when recording the thermal LSV signal. Scanning direction is from –y to +y (*i.e.* from bottom to top). The average distance between the device and bottom of the probe is 200 nm. The external magnetic field of 35 mT is applied along the –z direction to prevent the device from remagnetization, since the probe's field is ~ 40 mT in the +z direction, the resulting field immediately below the MB is 5 mT. As the coercive field of the device (obtained from Fig. 2(a)), is ~10 mT, *i.e.* larger than the accumulated external field, in this experiment the device has not been switched. Instead of different regions appearing as the probe scans over the surface (as in Fig. 3(a)), Fig. 3(c) shows two areas of locally/increase/decrease resistance centered at the metallic channel, a bright spot (maximum of ~ +0.1 Ω) when probe is near the emitter, and a dark spot (minimum of ~ -0.1 Ω) when the probe is

near the detector. This confirms that the signal measured in the thermal LSV depends on both emitter (*i.e.* AHE, bright spot) and detector (*i.e.* ANE effect, dark spot), and also that by partial compensation of the stray field of the probe it is possible to affect the device magnetization without reversing it.

IV. CONCLUSION

LSV made of ultra-thin Pt/CoFeB/Pt and operated in thermal mode has been studied by means of magnetotranspor measurements and SGM imaging using a MB attached to the scanning probe. The transport measurements demonstrate the sequential switching of the two magnetic elements that form the LSV (at ~ 10 and ~ 7 mT), evidencing that the magnetization can be tracked either by AHE or by using the thermal LSV configuration. As a non-magnetic element (Ta) with a very short spin-diffusion length was used as the channel, the thermal LSV signal implies a combination of ANE and AHE.

The DPC imaging of the modified probe shows that the MB field can be described using a dipole approximation (*i.e.* decays with z^3 from the center of the MB) with a field of about 85 mT on the surface of the probe and about 40 mT at a distance of 200 nm away from the MB.

By performing SGM in zero external field, it was demonstrated that the field from the MB switches the magnetization of the CoFeB elements as it hovers over them. Alternatively, by applying an external compensating magnetic field, we estimate the MB stray field intensity and directly measure its decay. The measurements performed in this way agree with the DPC results and the analytical model of a uniform magnetized sphere. Moreover, we demonstrate that by partial compensation of the MB stray field with an external field, it is possible to locally study the magnetization in this ultrathin film nanostructures. In particular, demonstrating that the output signal originates in this case as a combination of ANE and AHE.

ACKNOWLEDGMENTS

This work has been partially funded by EMRP and EMRP participating countries under Project EXL04 (SpinCal), EMPIR project 15SIB06 – Nanomag: Nano-scale traceable magnetic field measurements and FP7 project NanoMag. This work was also supported by the UK government's Department for Business, Energy and Industrial Strategy. We are very grateful to Tom Wren and James Wells for help with experiments and useful discussions.

[1] S. Hu and T. Kimura, Phys. Rev. B - Condens. Matter Mater. Phys. **90**, 134412 (2014).
[2] A. Hojem, D. Wesenberg, and B. L. Zink, Phys. Rev. B **94**, 024426 (2016).
[3] S. Hu, H. Itoh, and T. Kimura, NPG Asia Mater. **6**, e127 (2014).
[4] A. Slachter, F. L. Bakker, J.-P. Adam, and B. J. van Wees, Nat. Phys. **6**, 879 (2010).
[5] P. Laczkowski, L. Vila, V. D. Nguyen, A. Marty, J. P. Attané, H. Jaffrès, J. M. George, and A. Fert, Phys. Rev. B - Condens. Matter Mater. Phys. **85**, 220404 (2012).
[6] A. Slachter, F. L. Bakker, and B. J. van Wees, Phys. Rev. B **84**, 020412 (2011).
[7] H. Corte-León, B. Gribkov, P. Krzysteczko, F. Marchi, J.-F. Motte, H. W. Schumacher, V. Antonov, and O. Kazakova, J. Magn. Magn. Mater. **400**, 225 (2016).
[8] H. Corte-León, P. Krzysteczko, F. Marchi, J.-F. Motte, A. Manzin, H. W. Schumacher, V. Antonov, and O. Kazakova, AIP Adv. **6**, 056502 (2016).
[9] E. Montoya, P. Omelchenko, C. Coutts, N. R. Lee-Hone, R. Hübner, D. Broun, B. Heinrich, and E. Girt, Phys. Rev. B **94**, 054416 (2016).
[10] R. Mansell, A. Beguivin, D. C. M. C. Petit, A. Fernández-Pacheco, J. H. Lee, and R. P. Cowburn, Appl. Phys. Lett. **107**, 092405 (2015).
[11] J. Wells, J. H. Lee, R. Mansell, R. P. Cowburn, and O. Kazakova, J. Magn. Magn. Mater. **400**, 219 (2016).
[12] H. Corte-León, P. Krzysteczko, H. W. Schumacher, A. Manzin, D. Cox, V. Antonov, and O. Kazakova, J. Appl. Phys. **117**, 17E313 (2015).
[13] Magnequench, *January 8, 2009* (2009), ⟨http://www.mqitechnology.com/downloads/powder_datasheet_PDF/MQP-S-11-9-20001-070-pds.pdf⟩.
[14] S. McVitie and G. S. White, J. Phys. D. Appl. Phys. **37**, 280 (2004).
[15] S. McVitie, R. P. Ferrier, J. Scott, G. S. White, and A. Gallagher, J. Appl. Phys. **89**, 3656 (2001).
[16] R. P. Ferner, S. McVitie, A. Gallagher, and W. A. P. Nicholson, IEEE Trans. Magn. **33**, 4062 (1997).
[17] M. Jaafar, A. Asenjo, and M. Vázquez, IEEE Trans. Nanotechnol. **7**, 245 (2008).